Supporting Information

Near-Field Plasmonic Probe with Super Resolution and High Throughput and Signal-to-Noise Ratio

Ruei-Han Jiang,[†,‡,§] Chi Chen,[§] Ding-Zheng Lin,[‡] He-Chun Chou,[§] Jen-You Chu,[‡,*] Ta-Jen Yen[†,‡,*]

[†]Department of Materials Science and Engineering, National Tsing Hua University, Hsinchu 30013, Taiwan

[‡]Department of Materials and Chemical Research Laboratory, Industrial Technology and Research Institute, Hsinchu 31057, Taiwan

[§]Research Center for Applied Sciences, Academia Sinica, Taipei City, Taiwan

*Corresponding author e-mail address: tjyen@mx.nthu.edu.tw; RyanChu@itri.org.tw

S1 Plasmonic tip design

  1.1 Nanofabrication process of the plasmonic tip

  1.2 The enhancement improvement with optimal slits

  1.3 Tip apex observation (1) SEM image (2) Tip frontend reconstruction from AFM image

  1.4 Theoretical focus size at different tip apex diameter

S2 Near-field scanning optical measurement setup and throughput measurement of the a-tip and p-tip

S3 Characterizations of near-field signal contrast at the a-tip and p-tip

  3.1 Approaching curve on Au region of Fischer pattern

  3.2 Theoretical near field contrast

S4 Analysis of offset between the center of the inner plate and the intensity peak in the asymmetric and symmetric directions

S1 Plasmonic tip design

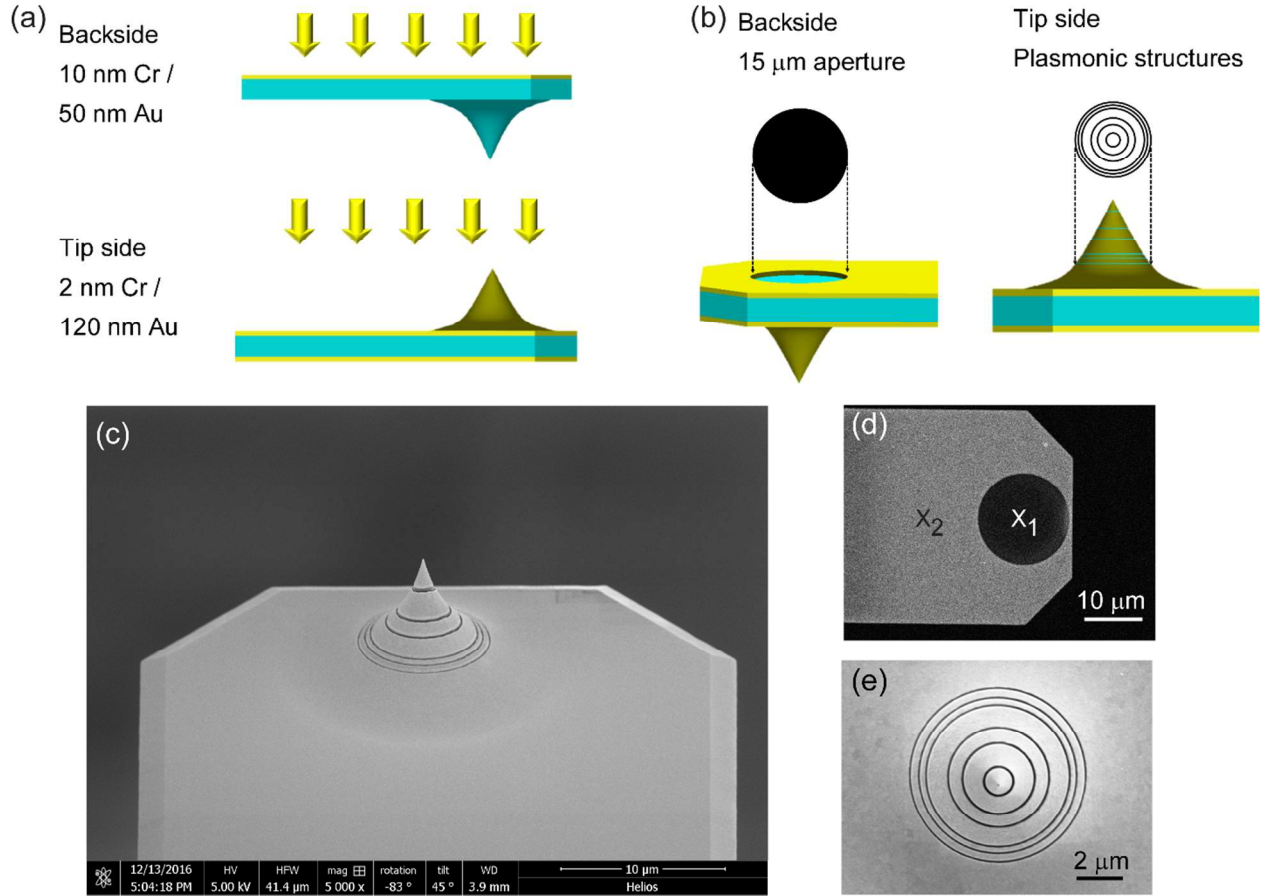### S1.1 Nanofabrication process of the plasmonic tip.

Figure S1. Fabrication method for the proposed plasmonic tip. (a) Metal deposition process: the following were deposited onto the SiO_2 tips: 10 nm Cr for adhesion, a 50 nm Au film on the backside, and a 2 nm Cr / 120 nm Au film on the tip side via DC sputtering. (b) Focus ion beam milling process: the black contour is the milling region on the tip side and backside. On the backside, the aperture was milled using a 40 nA current with a 30 kV Ga ion beam in the FEI Helios Nanolab 600i system. On the tip side, the plasmonic structure was milled using a 7.7 nA current with a 30 kV Ga ion beam. (c) SEM image of the proposed plasmonic tip: side view, (d)

backside view and (e) tip side view. Notably, position X_1 can allow the RP excitation light to transmit into the SiO_2 substrate, and the AFM feedback laser can be reflected by the remaining metal at position X_2 in the NSOM measurements.

In our experiment, excitation of the propagating SPPs onto the tip by free-space RP light was achieved using the plasmonic facet. The plasmonic facet efficiently coupled the incident light with a 100 nm annular trench and propagated the SPP wave onto the tip. The p-tips were prepared from a commercial SiO_2 probe (Nanosensor, uniqprobe®) with a tip apex of approximately 10 nm and an opening angle of ~ 18°. To obtain a chemically stable and low-loss metal film, Au has predominately been the material of choice for plasmonic applications at these optical frequencies. The 120 nm Au film and 5nm Cr film were deposited onto two sides of the SiO_2 probe via DC sputtering to obtain better film quality and step coverage (Figure S1a). The optimal plasmonic facet on the tip side and backside hole aperture on the Au film were milled using a focused ion beam (FEI Helios 660 Focused Ion Beam), as shown in Figure S1b. The fabricated plasmonic tip was well defined using a highly precise ion milling technique, as shown in Figure S1c. On the backside (Figure S1d), the aperture allowed the RP illumination to enter the SiO_2 material at position X_1, and the AFM feedback laser was reflected by the Au film at position X_2. On the tip side (Figure S1e), the groove width and depth of the ring were approximately 100 nm and 120 nm, respectively.

4

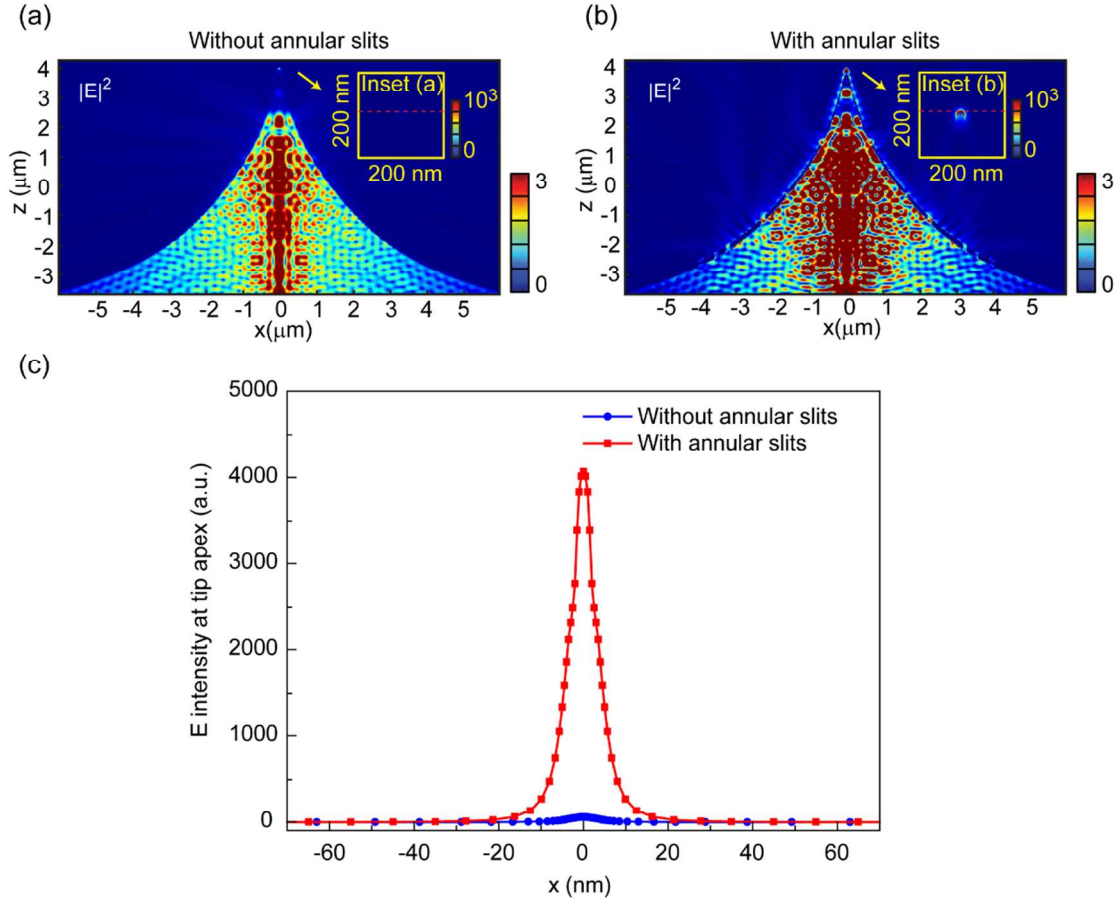### S.1.2 The enhancement improvement with optimal slits

Figure S2. The enhancement improvement with optimal slits (a) The $|E|^2$ distribution of the plasmonic tip without annular slits. The diameter of tip apex is 10 nm. (b) The $|E|^2$ distribution of the plasmonic tip with annular slits. The insets in (a) and (b) are the $|E|^2$ distribution at tip apex. (c) The intensity profile collected at 1 nm away from tip apex. The blue circle line and red square line are the cross sections of inset (a) and (b) respectively.

We deliberately designed six annular slits, with the sub-wavelength size at the specific locations. First, to solve the leakage radiations of annular slits, we narrowed down the slit width to subwavelength level. There is a weak total transmission for a subwavelength aperture due to

the scaling with $(w/\lambda)^4$.[1] In our case, the slits width (w) is 100 nm which is 1/6 times of wavelength. As a result, the total transmission (transmission plus scattering) is quite low. Moreover, when the exit of annular slit is node and the spacing between annular slits satisfied the integer number of surface plasmon wavelength, the scatter from annular slits could be minimized.[2] Herein, a direct comparison between the tip without and with slits are shown in Figure S2a (i.e., without slits) and Figure S2b (i.e., with slits), respectively. Referring to the dash-line in the inset (a) and (b), with the annular slits, we reach the enhancement up to 67 folds, indicated in Figure S2c.

S1.3 Tip apex observation of SEM image and tip frontend reconstruction from AFM image
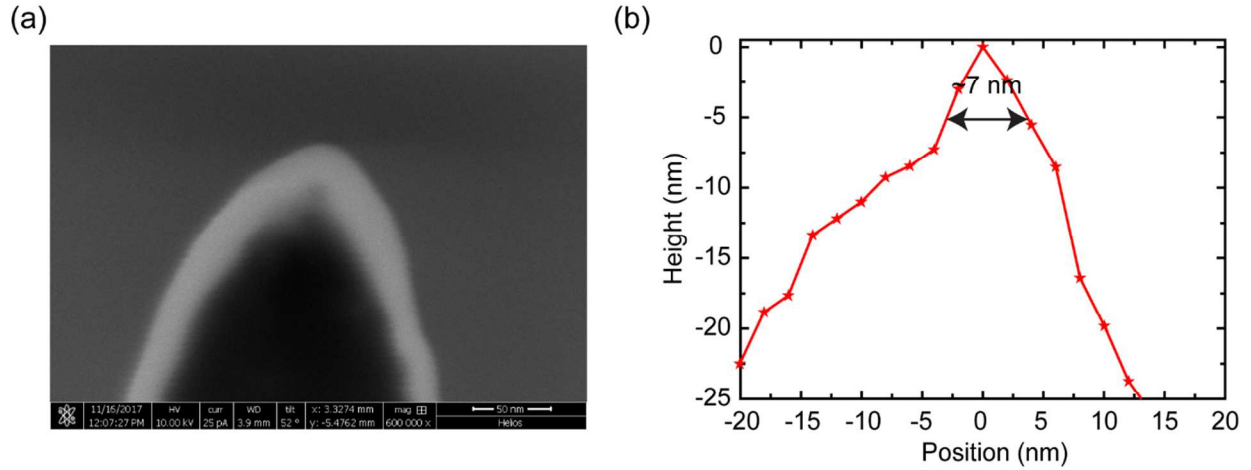
Figure S3 Tip apex observation: (a) High resolution SEM image (b) Tip frontend is reconstructed by blind tip reconstruction method (SPIP™ software)[3-6] from Fig. 2(e), the radius of curvature at tip apex is about 3.5nm.

To scrutinize our p-tip, we conducted a high-magnification SEM observation. As shown in Fig. 1(b) and Figure S3a, the p-tip was an apertureless type tip, and the tip apex was not broken after focused ion beam (FIB) milling. We intended to further examine the frontend protrusion of the p-tip because it is the region of the tip to scan the sample and to determine the resolution. However, we cannot acquire the precise dimension of the frontend protrusion during the high-magnification SEM observation, due to the charging effect that causes the blurry image (Fig. 1(b) and Figure S3a). Therefore, we adopted an AFM measurement on the tip, which can de-convolve the real size of the tip. We reconstructed the tip frontend by *blind tip reconstruction method* (SPIP™ software). [3-6] As shown Figure S3b, the radius of curvature at tip apex is about 3.5 nm.

S1.4 Theoretical focus size at different tip apex diameter

We simulated plasmonic tip with different tip apex with the same optimal annular slits. The crossline of focus spot at 1 nm distance away the tip apex is normalized by the maximum intensity of spot, as shown in Figure S4. Moreover, we calculated the focusing spot size in table S1. From table S1, the bigger tip apex would enlarge focusing spot size and decrease the local field at tip apex.
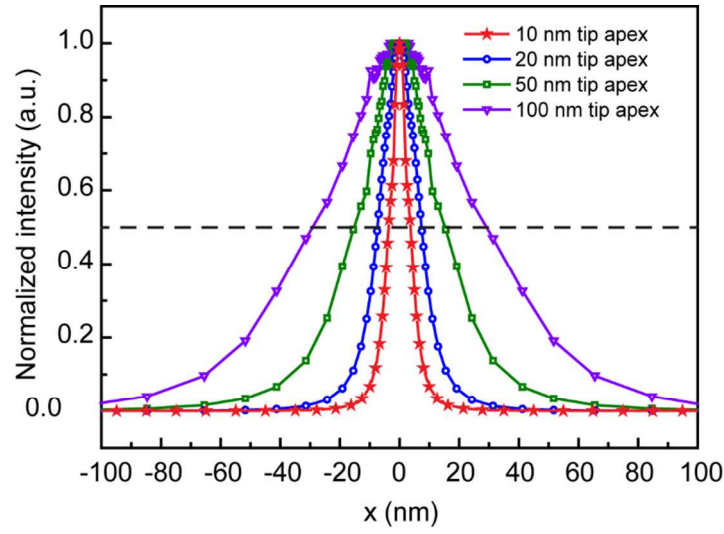

Figure S4. The theoretical focus size of different diameter tip apex

Table S1. The focusing spot size and E field intensity enhancement at different size tip apex

Tip apex diameter	100 nm	50 nm	20 nm	10 nm
Focusing spot size	59 nm	31 nm	15 nm	8 nm
E field intensity enhancement at tip apex	22	88	1056	4070

S2 Near-field scanning optical measurement setup and throughput measurement of the a-tip and p-tip
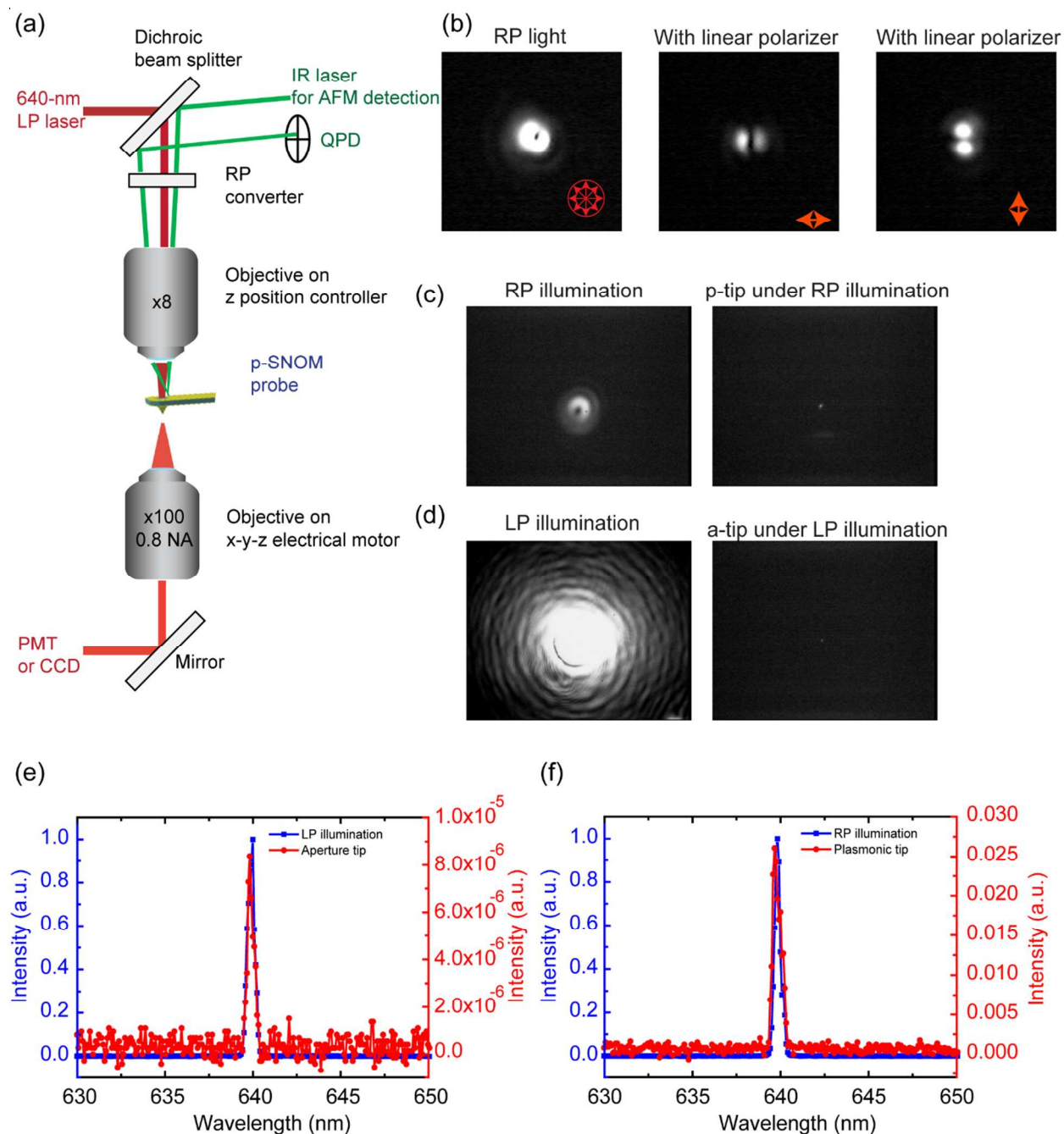

Figure S5. Near-field scanning optical measurement setup and throughput measurement of the a-tip and p-tip (a) NSOM measurement setup. (b) To detect the polarization direction of the RP light, we utilized a linear polarizer to filter the RP light. The linear polarizer is in the

horizontal direction, the dumbbell shape is symmetric, and the direction is along the linear polarizer direction. The same trend appears when the linear polarizer is in the vertical direction. The throughput measurement was demonstrated using the NSOM setup without a sample, and the downside lens was focused on the tip apex. (c) The CCD image of RP illumination and the p-tip under RP illumination in alignment with maximum intensity. (d) The CCD image of LP illumination and the a-tip under LP illumination in alignment with maximum intensity. Throughput measurement of the a-tip and p-tip : (e) the throughput of a-tip is normalized by intensity of LP illumination and (f) the throughput of p-tip is normalized by intensity of RP illumination.

The NSOM experiments were performed using a modified Witec NSOM system (Figure S5a). A diode-pumped solid-state laser (LASOS DPSS laser with 639.6 nm, spectral width ~ 1 nm, and polarization ratio > 200:1) served as the linearly polarized (LP) light source. Subsequently, the RP light (red line in Figure S5a) was transformed from LP light using a radial polarization converter (Altechna, RPC-632-06) and served as a light source parallel to the incident light with respect to the tip axis. We utilized the linear polarizer to confirm the polarization of the RP light (Figure S5b). The 980 nm laser (green line in Figure S5a) was reflected by the tip backside into the quadrant photodiodes detector for feedback control of the tip-sample distance, with piezo positioning stages for sample manipulation. In the alignment step, the p-tip holder was mounted onto a fine-tuning XY stage, allowing for precise positioning of the optical alignment between the RP light and p-tip. Therefore, we can obtain more degrees of freedom and thus tune the offset between the optical axis of the RP beam and the p-tip axis, in contrast to a fiber tip with the NSOM-AFM scheme. The light scattered from the tip was collected using a second objective (Nikon, 100X, numerical aperture of 0.8, working distance of 4.5 mm). The output signal was

sent to an image onto either a CCD camera or the entrance of an avalanche photo diode by switching the reflecting mirrors in the optical path. In the throughput measurement, the laser beam was focused onto the backside of the aperture of the p-tip to approximately 6 μm at normal incidence. After alignment, the SPP wave propagated to the tip and was coupled to far-field radiation via the antenna effect.

Under the condition of the plasmonic tip by RP light illumination, the strong scattered light could be observed only from the tip apex (Figure S5c). For the condition of aperture tip by LP light illumination, only weak scattered light could transmit through the aperture tip (Figure S5d). The output signal (c) and (d) was collected by Electron-Multiplying (EM) CCD camera (Spectrometer) with a 600-line grating   The throughput measurement is the ratio of the scattered light intensity from the tip to illumination which is derived from Figure S5e. and Figure S5f. In the far-field measurement, the p-tip exhibited a 3.28 % throughput under RP illumination and the a-tip exhibited a 7.03×10^{-4} % throughput under LP illumination.

S3 Characterizations of near-field signal contrast at the a-tip and p-tip

3.1 Approaching curve on Au region of Fischer pattern
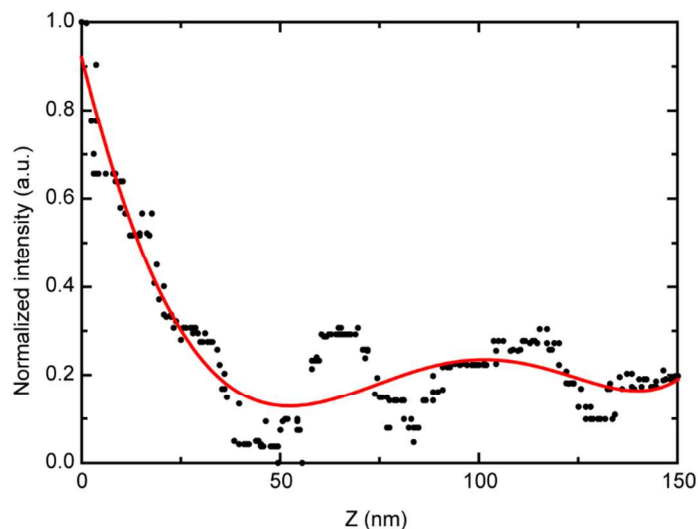

Figure S6. Collected p-NSOM signals on Au surface as a function of tip-sample distance (Z) by p-tip.

The approaching curve of the p-NSOM is collected on the Au region on Fisher's pattern, as shown in Figure S6, and the near-field signal decays when the tip is retracted. The Figure S6 could deduced the RP illumination is blocked by annular slits and the tip apex produce the near field source. Comparing with the approaching curves of traditional s-NSOM in the previous reports[7-9], because of the intensive scattering background from the substrate, the quality of those near-field images is so poor that researchers demanded to employ the 2nd harmonic order frequency modulation by lock-in amplifiers. In contrast, because of our nearly background-free near-field signal, we can adopt the zeroth order (DC) signal achieved to directly resolve unambiguous images.

3.2 Theoretical near field contrast

The near field source of p-tip is like the longitudinal dipole. As a result, the near field contrast of p-tip could be theoretically estimated by quasi-electrostatic dipole model.[10-12] Note that, the scattering intensity is proportional to $|\alpha_{eff}|^2$, which is calculated in accordance with the equation (3.3) in ref. S12, as tabulated in Table S2. In Table S2, the effective polarizability $|\alpha_{eff}|^2$ is calculated by collection of the far filed scattering light by dipole excitation by equation (3.3) in ref. S10. The results indicate that the near field signal of metal is larger than insulator (glass). In the Figure 2e, intensity on Au is higher than on SiO_2 substrate. The measurement data basically conforms to the dipole model. To further discuss the contrast of a-tip and p-tip, we simulated two case the p-tip is simplified to longitudinal dipole and a-tip is simplified to transversal dipole to check the contrast. And the transmission measurement setup is also considered. From Table S3 FDTD simulation results, the contrast of a-tip is Au < glass is matched with measurement data (Figure 2b). The contrast of p-tip is glass > Au is also matched with measurement data (Figure 2e). Simulation result analysis is qualitatively consistent with measurement.

Table S2. Calculated contrast by dipole model (Au tip, wavelength = 640 nm, distance of sample = 0 nm, tip apex radius = 5 nm, n_{glass}=1.52140, n_{Au}=0.168579+i 3.51508)

	Glass	Au	Result
$|\alpha_{eff}|^2$	1.04759×10^{-47}	4.98931×10^{-47}	$I_{Au} > I_{Glass}$

In addition to NSOM measurement, we also performed an SEM observation and found out similar contrast on the SiO_2 substrate, as shown in Figure. S7a. Additionally, we conducted an X-ray photoelectron spectroscopic (XPS) analysis as well, to probe the chemical composition on the very surface of the SiO_2 substrate. As shown in Figure. S7b, the result of XPS analysis suggested the contrast should be the residual PMMA on the SiO_2 substrate. To further confirm this result, we simulated three cases under both longitudinal dipole excitation and transversal dipole excitation at 640 nm wavelength: (1). triangle Au on glass, (2). PMMA on glass, and (3). bare glass. These confirmation results are summarized in Table S3. For longitudinal dipole excitation, the near-field brightness contrast gives rise to the following sequence: I_{Au} (1) > I_{PMMA}(0.152) > I_{Glass}(0); for transversal dipole excitation, the brightness contrast reveals the reverse sequence, I_{Glass} (1) > I_{PMMA}(0.912) > I_{Au}(0). In conclusion, our experimental analysis (Figure S8) and numerical simulation (Table S3) are all consistent; moreover, the contrast levels of SiO_2 and Au for the p-tip are even quantitatively match with the calculations from dipole model shown Table S2).
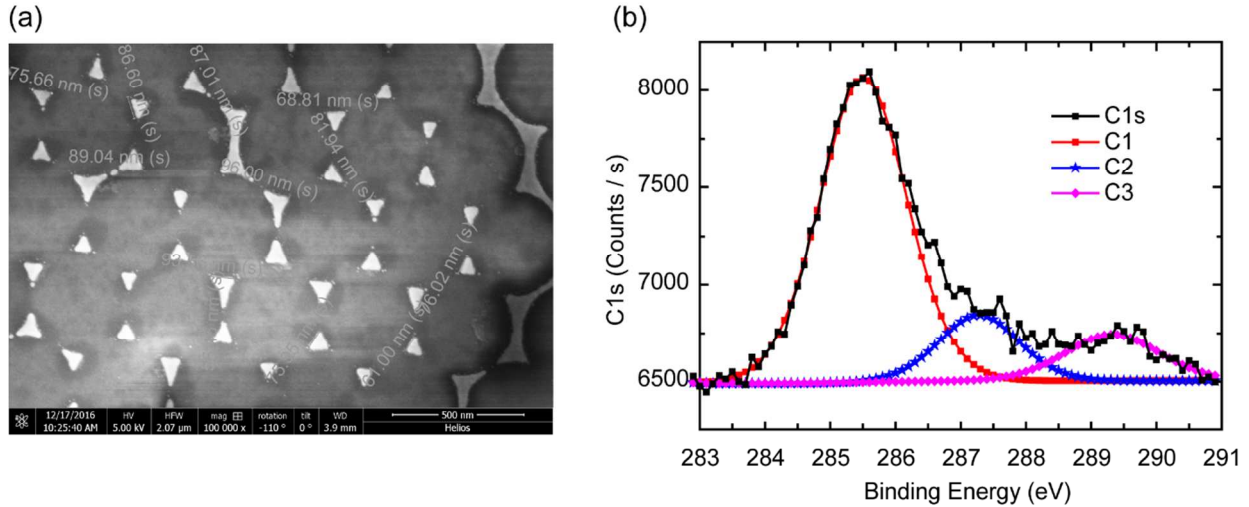

Figure S7 Characterizations of the residue PMMA on Fischer's pattern (a) SEM image and (b) XPS spectra of de-convoluted C1s envelopes of PMMA on the Fischer's pattern
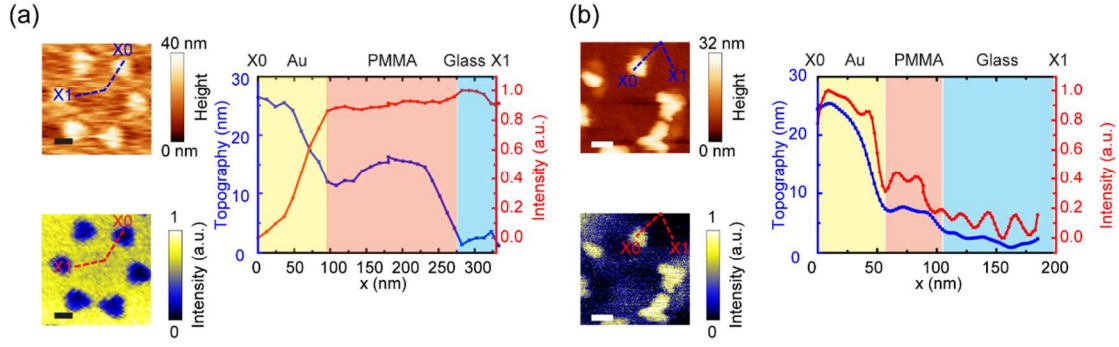
14

Figure S8. (a) Measured near field contrast of a-tip (b) Measured near field contrast of p-tip (Note: the scale bars in the figures denote 100 nm)

Table S3. Near field signal by FDTD simulations under the longitudinal dipole excitation and the transversal dipole excitation. (Detection angle ~ 30 degrees, n_{glass}=1.52140, n_{Au}=0.168579+i3.51508, n_{PMMA}=1.4884)

	Glass	Au on glass	PMMA on glass	Result
Longitudinal dipole excitation	5.03×10^{-4}	2.19×10^{-3}	5.35×10^{-4}	$I_{Au}(1) > I_{PMMA}(0.152) > I_{Glass}(1)$
Transversal dipole excitation	2.49×10^{-2}	8.46×10^{-3}	2.34×10^{-2}	$I_{Glass}(1) > I_{PMMA}(0.912) > I_{Au}(0)$

S4 Analysis of offset between the center of the inner plate and the intensity peak in the asymmetric and symmetric directions
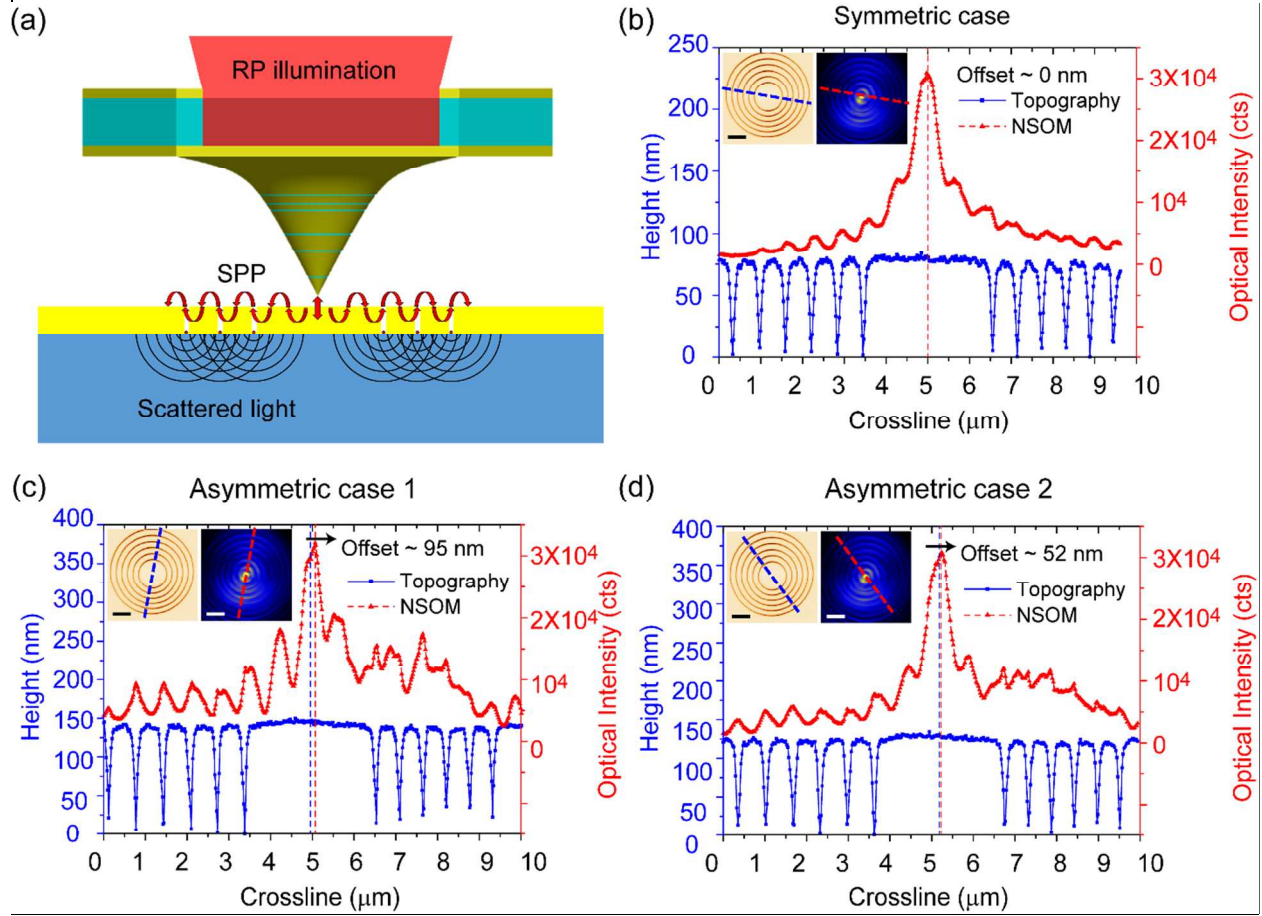

Figure S9. Surface plasmon interference of the asymmetric plasmonic lens. (a) Schematic of the asymmetric plasmonic lens measured using the p-tip. Symmetry case: (b) the focus spot was located at the center between the left grating (P ~ 601 nm) and right grating (P ~ 601 nm). Asymmetric cases: (c) the 95 nm offset of the focus shifted from the upper grating (P ~ 656 nm) to the lower grating (P ~ 558 nm). (d) The 52 nm offset of the focus shifted from the upper left (P ~ 648 nm) to the lower right (P ~ 571 nm). The blue and red lines in the figure denote the topography and corresponding NSOM cross-section, respectively. The blue and red dashed lines denote the center of the innermost ring and the position of the focal spot, respectively.
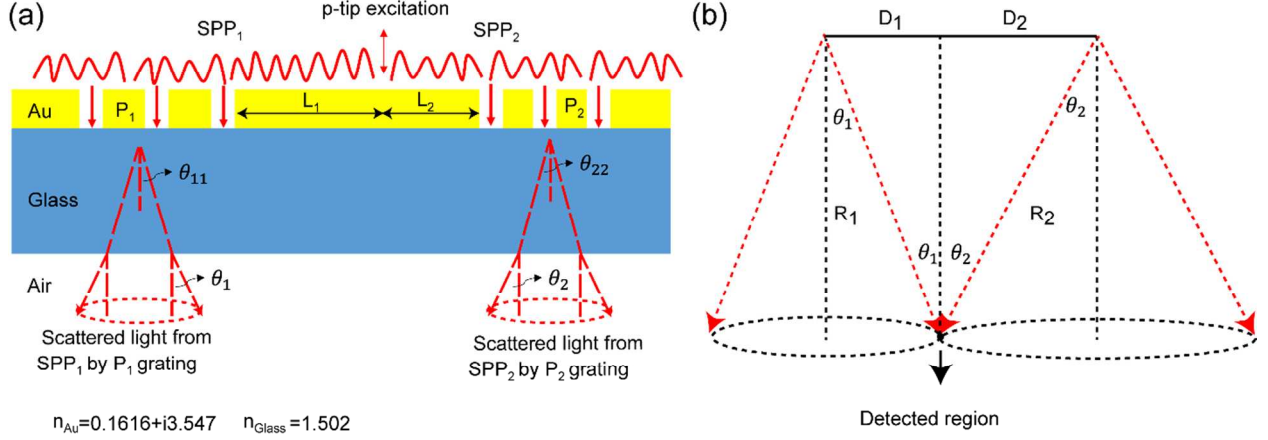
Figure S10. Focus offset calculation for the asymmetric plasmonic lens. (a) The intensity peak appeared in the asymmetric plasmonic lens when the scattered light from SPP_1 and SPP_2 produced constructive interference ($\Delta\emptyset = 0$). The dipole excited the SPP wave at the interface between Au and air. $\emptyset_{SPP_1}$ and $\emptyset_{SPP_2}$ are defined by the phase difference between the light scattered from SPP_1, SPP_2 and the reference point.

$$\emptyset_{SPP_1} = k_{spp}L_1 + \emptyset_{trench} + k_{1,glass}R_1$$

$\emptyset_{SPP_2} = k_{spp}L_2 + \emptyset_{trench} + k_{2,glass}R_2$ where $k_{spp} = \frac{\omega}{c}\sqrt{\frac{\varepsilon_m\varepsilon_d}{\varepsilon_m+\varepsilon_d}} = \frac{2\pi}{\lambda_{spp}}$, with λ_{spp} at the air/Au interface = 614 nm for an excitation wavelength of 640 nm. SPP_1 and SPP_2 were scattered by the grating structures. We calculated $k_{1,glass}$ and $k_{2,glass}$ for the reciprocity case. The light in the glass with the grating coupling excited the SPP wave at the interface between air and the gold film, as shown below.

$$k_{1,glass} = n_{glass}\frac{\omega}{c}\sin\theta_{11} = \frac{\omega}{c}\sqrt{\frac{\varepsilon_m\varepsilon_d}{\varepsilon_m+\varepsilon_d}} \pm m\frac{2\pi}{p} = \frac{2\pi}{\lambda_{spp}} - m\frac{2\pi}{P_1}$$

$$k_{2,glass} = -n_{glass}\frac{\omega}{c}\sin\theta_{22} = \frac{\omega}{c}\sqrt{\frac{\varepsilon_m\varepsilon_d}{\varepsilon_m+\varepsilon_d}} \pm m\frac{2\pi}{p} = \frac{2\pi}{\lambda_{spp}} - m\frac{2\pi}{P_2}$$

(b) According to Snell's law, i.e., $n_{glass}\sin\theta_{11} = n_{Air}\sin\theta_1$ and $n_{glass}\sin\theta_{22} = n_{Air}\sin\theta_2$, we calculated the equivalent optical path difference of the light scattered from SPP_1 and SPP_2 in

air. The light path difference $= R_2 - R_1 = \frac{D_2}{\sin\theta_2} - \frac{D_1}{\sin\theta_1}$.

Table S4 Comparison between the theoretical calculations and measurement results for $\boldsymbol{d_{offset}}$

	P1	P2	d_{offset}	Measured d_{offset}
Figure S4b	601 nm	601 nm	0 nm	0 nm
Figure S4c	656 nm	558 nm	91.5 nm	95 nm
Figure S4d	648 nm	571 nm	57.3 nm	52.4 nm

We define $2d_{offset} = L_1 - L_2, D_1:D_2 = \tan\theta_1:\tan\theta_2, D_1 + D_2 = detection\ area = 10\ \mu m$.

For constructive interference, $\Delta\emptyset = \emptyset_{SPP_1} - \emptyset_{SPP_2} = k_{spp}(L_1 - L_2) + k_{Air}(R_1 - R_2) = 0$. Using

the formula $d_{offset} = \frac{k_{Air}}{2k_{spp}}(R_2 - R_1)$, we calculated d_{offset}, as shown in Table S1.

REFERENCES

[S1] Maier, S. A. Plasmonics: *Fundamentals and Applications*; Springer: Berlin, **2007**

[S2] Pacifici, D.; Lezec, H. J.; Weiner, J.; Atwater, H. *A. Phys. Rev. B* **2008** 77 115411

[S3] Mazeran, P. E.; Odoni, L.; Loubet, J. L. *Surf. Sci.* **2005**, *585*, 25.

[S4] Colombi P.; Alessandri I.; Bergese P.; Federici S.; Depero L. E. *Measurement Science and Technology* **2009**, *20*, 084015.

[S5] Gotszalk, T. P.; Henrykowski, A.; Józwiak, G.; Masalska, A.; Ritz, I.; Steigmann, H. *CoRR* **2011**, abs/1105.1472.

[S6] Dongmo L. S.; Villarrubia J. S.; Jones S. N.; Renegar T. B.; Postek M. T.; Song J. F. *Ultramicroscopy* **2000**, *85*, 141.

[S7] Chu, J. Y.; Wang, J. K. *Advanced Photonic Sciences* **2012**.

[S8] Keilmann, F.; Hillenbrand, R. *Phil. Trans. R. Soc. London A* **2004**, *362*, 787.

[S9] Bek, A.; Vogelgesang, R.; Kern, K. *Appl. Phys. Lett.* **2005**, *87*, 163115.

[S10] Keilmann, F.; Hillenbrand, R. *Phil. Trans. R. Soc. London A* **2004**, *362*, 787.

[S11] Cvitkovic, A.; Ocelic, N.; Hillenbrand, R. *Opt. Express* **2007**, *15*, 8550.

[S12] Chu, J. Y.; Wang, J. K. *Advanced Photonic Sciences* **2012**.